

# A PAndAS view of M31 dwarf elliptical satellites: NGC147 and NGC185

D. Crnojević<sup>1,2\*</sup>, A. M. N. Ferguson<sup>1</sup>, M. J. Irwin<sup>3</sup>, A. W. McConnachie<sup>4</sup>, E. J. Bernard<sup>1</sup>, M. A. Fardal<sup>5</sup>, R. A. Ibata<sup>6</sup>, G. F. Lewis<sup>3,7</sup>, N. F. Martin<sup>6</sup>, J. F. Navarro<sup>8</sup>, N. E. D. Noël<sup>9</sup>, S. Pasetto<sup>10</sup>

<sup>1</sup>*Institute for Astronomy, University of Edinburgh, Royal Observatory, Blackford Hill, EH9 3HJ Edinburgh, UK*

<sup>2</sup>*Physics Department, Texas Tech University, Lubbock, TX 79409, USA*

<sup>3</sup>*Institute of Astronomy, University of Cambridge, Madingley Road, CB3 0HA Cambridge, UK*

<sup>4</sup>*NRC Herzberg Institute of Astrophysics, 5071 West Saanich Road, Victoria, BC, V9E 2E7, Canada*

<sup>5</sup>*Department of Astronomy, University of Massachusetts, Amherst, MA 01003, USA*

<sup>6</sup>*Observatoire astronomique de Strasbourg, Université de Strasbourg, CNRS, UMR 7550, 11 rue de l'Université, F-67000 Strasbourg, France*

<sup>7</sup>*Sydney Institute for Astronomy, School of Physics A28, The University of Sydney, NSW 2006, Australia*

<sup>8</sup>*Department of Physics and Astronomy, University of Victoria, Victoria, BC, Canada*

<sup>9</sup>*Department of Physics, University of Surrey, GU2 7XH Guildford Surrey, UK*

<sup>10</sup>*University College London, Department of Space & Climate Physics, Mullard Space Science Laboratory, Holmbury St. Mary, RH5 6NT Dorking Surrey, UK*

Accepted 2014 September 24. Received 2014 September 21; in original form 2014 July 12

## ABSTRACT

We exploit data from the Pan-Andromeda Archaeological Survey (PAndAS) to study the extended structures of M31's dwarf elliptical companions, NGC147 and NGC185. Our wide-field, homogeneous photometry allows to construct deep colour-magnitude diagrams (CMDs) which reach down to  $\sim 3$  mag below the red giant branch (RGB) tip. We trace the stellar components of the galaxies to surface brightness of  $\mu_g \sim 32$  mag arcsec<sup>-2</sup> and show they have much larger extents ( $\sim 5$  kpc radii) than previously recognised. While NGC185 retains a regular shape in its peripheral regions, NGC147 exhibits pronounced isophotal twisting due to the emergence of symmetric tidal tails. We fit single Sersic models to composite surface brightness profiles constructed from diffuse light and star counts and find that NGC147 has an effective radius almost 3 times that of NGC185. In both cases, the effective radii that we calculate are larger by a factor of  $\sim 2$  compared to most literature values. We also calculate revised total magnitudes of  $M_g = -15.36 \pm 0.04$  for NGC185 and  $M_g = -16.36 \pm 0.04$  for NGC147. Using photometric metallicities computed for RGB stars, we find NGC185 to exhibit a metallicity gradient of  $[\text{Fe}/\text{H}] \sim -0.15$  dex/kpc over the radial range 0.125 to 0.5 deg. On the other hand, NGC147 exhibits almost no metallicity gradient,  $\sim -0.02$  dex/kpc from 0.2 to 0.6 deg. The differences in the structure and stellar populations in the outskirts of these systems suggest that tidal influences have played an important role in governing the evolution of NGC147.

**Key words:** galaxies: Local Group - galaxies: dwarf - galaxies: evolution - galaxies: individual: NGC147, NCG185 - galaxies: photometry - galaxies: stellar content

## 1 INTRODUCTION

Dwarf galaxies have long been considered relatively simple objects due to their small sizes. However, detailed studies of our Local Group (LG) dwarf members have unveiled a great degree of complexity in their resolved stellar populations and star formation histories (SFHs; e.g., Grebel 1997; Mateo 1998; van den Bergh

1999). Discrepancies between their observed properties and theoretical predictions have often been used to argue against the widely-accepted  $\Lambda$  CDM model, although uncertainties in modelling baryonic physics may also play a role (for a recent discussion see e.g., Weinberg et al. 2013). Nonetheless, dwarf galaxies are exciting testbeds for refining our view of galaxy formation and evolution, and represent a vital step in the understanding of more massive and complex objects.

As a result of their small masses, dwarf galaxies are particu-

\* Email: denija.crnojevic@ttu.edu

**Table 1.** Assumed properties of NGC147 and NGC185. Columns are (1): name of the galaxy; (2-3): equatorial coordinates from the NED database (<http://ned.ipac.caltech.edu/>); (4-5) Galactic longitude and latitude (NED); (6) absolute  $V$  magnitude, obtained using the apparent, de-reddened magnitude listed in NED (originally from de Vaucouleurs et al. 1991) and the distance modulus derived by Conn et al. (2012); (7-9): apparent TRGB  $i$ -band magnitude and deprojected distances from the Milky Way and from M31 (Conn et al. 2012, uncertainties stem from the resulting Posterior Probability Distributions); (10-11): mean extinction values (SDSS bands) from NED; (12-13): mean position angle (measured from north through east) and ellipticity as derived in this study (see Sect. 4).

Galaxy	$\alpha_{J2000}$ ( $^h m^s$ )	$\delta_{J2000}$ ( $^{\circ} ' ''$ )	$l$ (deg)	$b$ (deg)	$M_V$ (mag)	$m_{i,TRGB}$ (mag)	$d_{MW}$ (kpc)	$d_{M31}$ (kpc)	$A_g$ (mag)	$A_i$ (mag)	$PA$ ( $^{\circ}$ )	$\epsilon$
NGC147	00 33 12.12	48 30 31.5	119.82	-14.25	-15.33	$20.82^{+0.08}_{-0.08}$	$712^{+21}_{-19}$	$118^{+15}_{-15}$	0.570	0.293	$34.2 \pm 3.6$	$0.46 \pm 0.02$
NGC185	00 38 57.97	48 20 14.6	120.79	-14.48	-15.41	$20.52^{+0.09}_{-0.08}$	$620^{+19}_{-18}$	$181^{+25}_{-20}$	0.608	0.313	$45.9 \pm 1.2$	$0.22 \pm 0.01$

larly sensitive to processes that affect gas content, and thus star formation, and both internal feedback and environmental effects are likely to play major roles in governing their evolution. For example, the origin of dwarf elliptical (dE) galaxies is a longstanding question: are they simply scaled-down versions of more massive early-type galaxies, which experience the main episode of star formation at early epochs, or do they result from the morphological transformation of gas-rich dwarf irregular (dIrr) galaxies which are depleted of their gas content through environmental processes (e.g., ram-pressure stripping, tidal interactions)? The role of internal versus environmental factors has been discussed extensively in the literature (see, e.g., Mateo 1998; Grebel et al. 2003) but there is as of yet no consensus. Investigating the structural profiles and stellar populations gradients in these systems has the potential to help distinguish between possible origins.

It is within the LG that the resolved stellar populations of dwarf galaxies can be studied with the greatest precision. Only four dE galaxies are known within the LG (NGC185, NGC147, NGC205 and M32) and all of these are likely satellites of M31. Lying in M31’s remote halo, NGC185 and NGC147 were first recognised as LG members by Baade (1944). Accurate distances, derived with the tip of the red giant branch (TRGB) method, place NGC185 at  $\sim 620$  and NGC 147 at  $\sim 710$  kpc from us<sup>1</sup>, and at  $\sim 180$  and  $\sim 120$  kpc from the centre of M31 (Conn et al. 2012, see Tab. 1). Their 3D separation is only  $93 \pm 27$  kpc and they have heliocentric radial velocities of  $\sim -203$  km/s and  $\sim -193$  km/s, respectively (Geha et al. 2010). There has been much debate about whether they form a physical system or not (e.g. van den Bergh 1998; Watkins et al. 2013; Fattahi et al. 2013; Evslin 2014). Despite having similar luminosities, the two dEs show some marked differences in their internal properties. NGC 185 hosts a population of young stars, some of which formed as recently as  $\sim 100$  Myr ago (e.g. Martínez-Delgado et al. 1999). It also has central dust lanes and  $\sim 3.0 \times 10^5 M_{\odot}$  of neutral gas, an amount that is consistent with stellar mass loss originating from the most recent star formation event (Marleau et al. 2010). On the other hand, NGC147 does not contain significant dust or gas, and shows no evidence for a population younger than  $\sim 1$  Gyr (e.g. Sage et al. 1998; Marleau et al. 2010). The mean metallicities and metallicity gradients have been investigated in both systems with varying conclusions, possibly reflecting the different analysis methods and areal coverages of the individual studies (e.g. Han et al. 1997; Martínez-Delgado et al. 1999; Battinelli & Demers 2004b,a; Gonçalves et al. 2007; Geha et al. 2010; Gonçalves et al. 2012; Ho et al. 2014). A recent spectroscopic study of NGC185 and

NGC147 probed stellar kinematics to large radii and discovered significant rotation in both galaxies (Geha et al. 2010), contrary to what had been previously found by smaller FoV studies (Bender et al. 1991; Simien & Prugniel 2002). This provides important insight into the formation mechanism of this class of galaxies, suggesting a rotationally-supported origin possibly followed by a morphological transformation.

In this work, we present a photometric analysis of the stellar content of NGC147 and NGC185 derived from very wide-field survey data. Many galaxies have recently been shown to have large low surface brightness extensions (e.g. Barker et al. 2012; Bernard et al. 2012; Crnojević et al. 2013; Ibata et al. 2014), the properties of the which hold important clues to their past histories, and it is natural to ask whether these two systems do too. We exploit data from the Pan-Andromeda Archaeological Survey (PAndAS) that imaged the M31 halo out to projected distances of  $\sim 150$  kpc (McConnachie et al. 2009) and which provides deep uniform photometry out to unprecedented radii for both dwarfs. This dataset has already led to the discovery of a prominent stellar stream emanating from NGC147, which is reported in detail elsewhere (e.g., Ibata et al. 2014; Martin et al. 2013, Irwin et al., in prep.), as well as several new globular clusters around both systems (Veljanoski et al. 2013). In this paper, we analyse the resolved stellar populations across large swaths of the two dEs and re-examine their extents, structural properties and chemical contents.

The paper is organized as follows: in §2 we present the data and the photometry, and show the resulting colour-magnitude diagrams (CMDs) in §3. We analyse the spatial distribution of populations in §4, their radial density and surface brightness profiles in §5, while in §6 we derive photometric metallicity distribution functions (MDFs) and investigate the metallicity gradients. We discuss our results in §7, and draw our conclusions in §8.

## 2 OBSERVATIONS AND PHOTOMETRY

The PAndAS survey was conducted with the MegaPrime/MegaCam camera on the 3.6 m Canada-France-Hawaii Telescope (CFHT) under excellent average seeing conditions ( $< 0.8''$ ). MegaCam consists of a mosaic of 36  $2048 \times 4612$  CCDs with a total FoV of  $\sim 1 \times 1$  deg<sup>2</sup> and pixel scale  $0.187''$  per pixel. The effective area covered by each pointing is about  $0.96 \times 0.94$  deg<sup>2</sup> due to small gaps between the chips. In total, roughly 400 deg<sup>2</sup> was mapped around M31 and M33 via 413 distinct MegaCam pointings. The observing strategy, data processing and calibration have been fully described elsewhere (McConnachie et al. 2009, 2010; Richardson et al. 2011; Ibata et al. 2014).

<sup>1</sup> At these distances, 1 kpc=5.6 arcmin (NGC185) and 1 kpc=4.8 arcmin (NGC147).

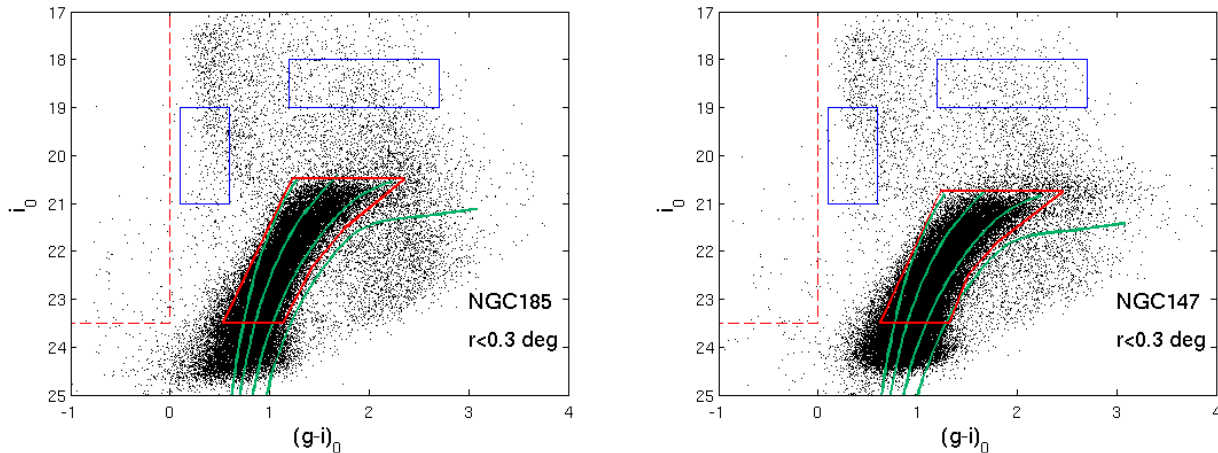


**Figure 1.** De-reddened CMDs of the dEs, showing only stars falling within an ellipse of semi-major axis 0.3 deg. Overlaid are Dartmouth isochrones (green lines) with a fixed age of 12 Gyr and varying metallicity ( $[\text{Fe}/\text{H}] = -2.5, -1.3, -0.7$  and  $-0.3$ ), shifted to the appropriate distance. The adopted RGB boxes are outlined in red, while blue boxes indicate areas dominated by foreground sequences (Galactic halo:  $0.1 < (g-i)_0 < 0.6$ ,  $19 < i_0 < 21$ ; Galactic disc:  $1.2 < (g-i)_0 < 2.7$ ,  $18 < i_0 < 19$ ). The dash-dotted red line isolates candidate young stars. We do not consider luminous AGB stars in this work as their study is deferred to a future paper incorporating a NIR dataset.

As a brief summary, the raw data are pre-processed through the *Elixir* CFHT pipeline, and the source detection and aperture photometry are obtained with the CFHT/MegaPrime adapted version of the Cambridge Astronomical Survey Unit (CASU) pipeline (Irwin & Lewis 2001). PSF-fitting photometry is subsequently performed using DAOPHOT/ALLSTAR (Stetson 1987). Although PSF-fitting photometry leads to smaller photometric uncertainties (see Ibata et al. 2014), the quality of fit parameters vary greatly between CCDs and thus cannot be used to clean our catalogue of non-stellar sources. Instead, the PSF photometry and the CASU aperture photometry are cross-matched and the source classifications from the latter are adopted. For the bulk of our analysis, only objects classified as stellar or probably stellar (i. e. within  $2\sigma$  of the stellar locus; Irwin & Lewis 2001) in both bands are used. The resulting  $g$  and  $i$  magnitudes are on the AB system, and the final band-merged catalogue provides both morphological classification and accurate astrometry for each source. Sources in our catalogue have a signal-to-noise ratio of  $\sim 5$  (corresponding to a photometric error of 0.2 mag) at  $i_0 \sim 24 - 24.5$  and  $g_0 \sim 25 - 25.5$ .

Throughout this study we use de-reddened magnitudes, adopting the extinction values obtained from the Schlegel et al. (1998)  $E(B-V)$  maps interpolated on a star-by-star basis. Additionally, we apply the Bonifacio et al. (2000) correction for  $E(B-V) > 0.1$  (their formula 1), which returns slightly smaller values than the original ones. The mean extinction for a  $\sim 3 \times 3 \text{ deg}^2$  field centered on NGC185 and NGC147 is  $\langle E(B-V) \rangle \sim 0.13$  and presents spatial variations of up to  $\sim 40\%$ . We apply the following conversion to obtain the final de-reddened magnitudes:  $g_0 = g - 3.793 E(B-V)$  and  $i_0 = i - 2.086 E(B-V)$  (Schlegel et al. 1998).

Tab. 1 lists the properties of the two dwarf galaxies. The distance to the dEs is taken from Conn et al. (2012), which has been derived from the TRGB luminosity via a Bayesian approach using the same PAndAS dataset. We have recomputed the position angle  $PA$ , ellipticity  $\epsilon$  and effective radius  $r_{\text{eff}}$  for each galaxy, given the larger extent of our data with respect to previous surveys (details in Sect. 4). Throughout this paper, we use standard coordinates (centered on either NGC185 or NGC147) and refer to galactocentric

projected elliptical radii ( $r = \sqrt{x^2 + y^2 / (1 - \epsilon^2)}$ ) computed using our mean values of position angle ( $PA$ ) and  $\epsilon$ .

### 3 COLOUR-MAGNITUDE DIAGRAMS

In Fig. 1 we show de-reddened colour-magnitude diagrams (CMDs) for NGC185 and NGC147. We plot all stars in each system lying within an ellipse of semi-major axis 0.3 deg to highlight the main CMD sequences. The most prominent feature in the CMDs is a broad red giant branch (RGB), indicative of old ( $\sim 2$  to 13 Gyr) populations that have evolved off the main sequence (MS). Dartmouth isochrones in the CFHT photometric system (Dotter et al. 2008; McConnachie et al. 2010) have been overlaid on the RGB. The isochrones have been shifted to the distance of each galaxy and have an age of 12 Gyr,  $[\alpha/\text{Fe}] = +0.0$  and varying metallicity to encompass the full width of the RGB. For our subsequent analysis, we define a selection box on the main RGB locus with the bright limit set by the TRGB luminosity and a faint limit of  $i_0 = 23.5$ . The faint limit has been chosen to limit incompleteness in our data and minimise contamination from unresolved galaxies which become significant at magnitudes fainter than this (see Ibata et al. (2014) and Fig. 3).

The other main features visible in the CMDs are due to foreground stars which are especially prominent given the low Galactic latitude of the two systems. The almost vertical sequence at  $0.2 \lesssim (g-i)_0 \lesssim 1.0$  and  $g_0 \lesssim 21$  results from halo turnoff stars, while the broad diagonal sequence with  $1.5 \lesssim (g-i)_0 \lesssim 3.0$  is due to disc dwarfs. Short-lived, luminous asymptotic giant branch (AGB) stars are expected to be found above the TRGB and are indicative of intermediate-age populations ( $\sim 0.5 - 8$  Gyr). Such populations are indeed visible up to  $\sim 1$  mag above the TRGB and redward of the RGB box, at colours  $1.5 \lesssim (g-i)_0 \lesssim 3$ , especially for NGC147. However, this region of the CMD is significantly contaminated by foreground stars in optical bands, such that an accurate analysis of AGB stars is not feasible from the PAndAS data alone. We defer the study of intermediate-age populations in the target dEs to a fu-

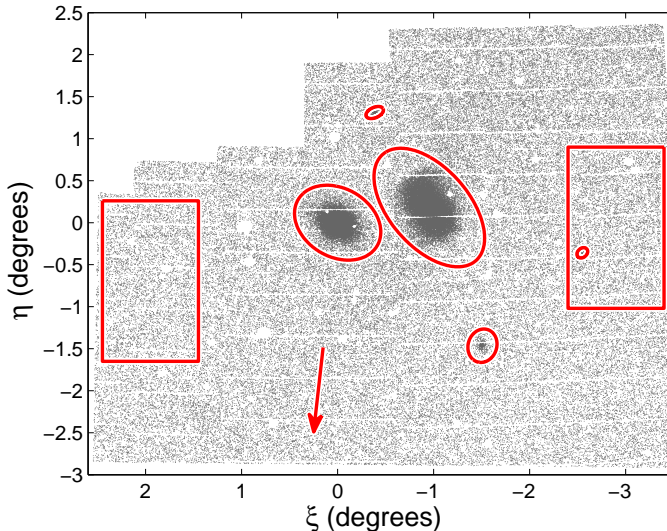


**Figure 2.** Spatial distribution of sources falling within the NGC185 RGB box (in standard coordinates centered on NGC185). North is up and east is left. The red boxes indicate the position of the two adopted field regions (each covering a  $\sim 1.9 \text{ deg}^2$  area) used to monitor contaminants. Large red ellipses are drawn with radii of 0.5 deg around NGC185 (left) and 0.8 deg around NGC147 (right). Also shown are the dwarf spheroidal galaxies Cass II ( $\xi = -0.39^\circ$ ,  $\eta = 1.31^\circ$ ), And XXV ( $\xi = -1.51^\circ$ ,  $\eta = -1.46^\circ$ ) and And XXVI ( $\xi = -2.55^\circ$ ,  $\eta = -0.36^\circ$ ), where the ellipse in each case indicates  $4r_{\text{eff}}$ . The arrow points in the direction of M31.

ture paper which will also incorporate near-infrared (NIR) data, enabling a cleaner and more robust separation from foreground stars.

Finally, a few objects are visible at colours bluer than  $(g-i)_0 \lesssim 0$  (vertical dashed line in Fig. 1), suggesting the presence of young, massive MS stars. While NGC185 has been previously shown to have signs of recent star formation in its main body (Lee et al. 1993; Martínez-Delgado et al. 1999; Butler & Martínez-Delgado 2005; Marleau et al. 2010), NGC147 is not known to contain young stars. Some foreground stars could contaminate this CMD region, however. We define a selection box for blue stars at  $-1.0 < (g-i)_0 < 0.0$ ,  $17 < i_0 < 23.5$  and consider in detail their spatial distribution in the following analysis, though we note that crowding in the central regions – where these sources typically lie – limits straightforward interpretation.

### 3.1 Foreground/background contamination

While our photometric catalogue will be dominated by stars in NGC147 and NGC185, there will also be contaminant sources. Accounting for these is crucially important when analysing the low surface density peripheral regions of the two dwarfs. There are three types of contaminating sources to consider – Galactic foreground stars, M31 halo stars, and unresolved background galaxies. While M31 halo stars and background galaxies are expected to be relatively smoothly distributed over our FoV (we are considering large galactocentric distances from M31 where the halo density falls off slowly, Ibata et al. 2014), the contribution from Galactic disc stars significantly increases in the north-west direction due to the low Galactic latitude ( $b \sim -14^\circ$ ) of the systems.

In order to account for contaminants, we select two large rectangular “field” regions that lie east and west of the dEs (see Fig. 2), each with an area of  $\sim 1.9 \text{ deg}^2$ . These large areas minimise sensitivity to any possible localized substructure in M31’s halo. The east region contains  $\sim 75000$  stars, while the west region contains  $\sim 85000$  stars; this difference is in the right sense to be consistent

with gradient in foreground density due to the Galactic disc. Our field regions are chosen to avoid the north-south direction because of the presence of NGC147’s extended tidal tails and the dwarf spheroidal galaxies Cass II (Irwin et al., in prep.) and And XXV (Richardson et al. 2011). A third low-mass galaxy, And XXVI (the least luminous of the three), lies within our west field region but we have excised stars falling within a  $4 r_{\text{eff}}$  ellipse centered on this dwarf (there are virtually no stars belonging to And XXVI outside this radius).

The CMD of the combined field regions is shown in the left panel of Fig. 3, scaled to an arbitrary area of  $0.25 \text{ deg}^2$  to ease the identification of the main features. This is comparable to the surveyed area within  $r = 0.3 \text{ deg}$  (after gap subtraction) for NGC185 ( $\sim 0.20 \text{ deg}^2$ ) and NGC147 ( $\sim 0.27 \text{ deg}^2$ ) and hence should represent the level of contamination present in the CMDs of Fig. 1. Besides the prominent foreground sequences, sources found at magnitudes greater than  $i_0 \sim 23.5$  (i.e. below our RGB box faint limit) are largely unresolved background galaxies (see, e.g., Fig 9 of Barker et al. 2012). The RGB of M31’s stellar halo is barely visible due to its low density at these galactocentric radii. Finally, a few sources bluer than  $(g-i)_0 \sim 0$  are also present, representing an important source of contamination for the identification of possible young stars belonging to the dEs.

The right panel of Fig. 3 shows the Galactic foreground in the direction of NGC185 and NGC147 as predicted by the Besançon model (Robin et al. 2003). Stars have been simulated over an area of  $2.5 \text{ deg}^2$  centered at an  $(l, b)$  that lies between the two dwarfs and subsequently convolved with the observational errors from our photometry (as a function of magnitude only). We have not applied a correction for incompleteness. From the final catalogue of foreground contaminants, we extract a subset of stars by scaling their numbers to an area of  $0.25 \text{ deg}^2$  in order to match the left panel of Fig. 3. The simulated foreground sequences are broadly in agreement with the observed ones. We consider stars from the observed field CMD within the same RGB selection boxes drawn in Fig. 1 as

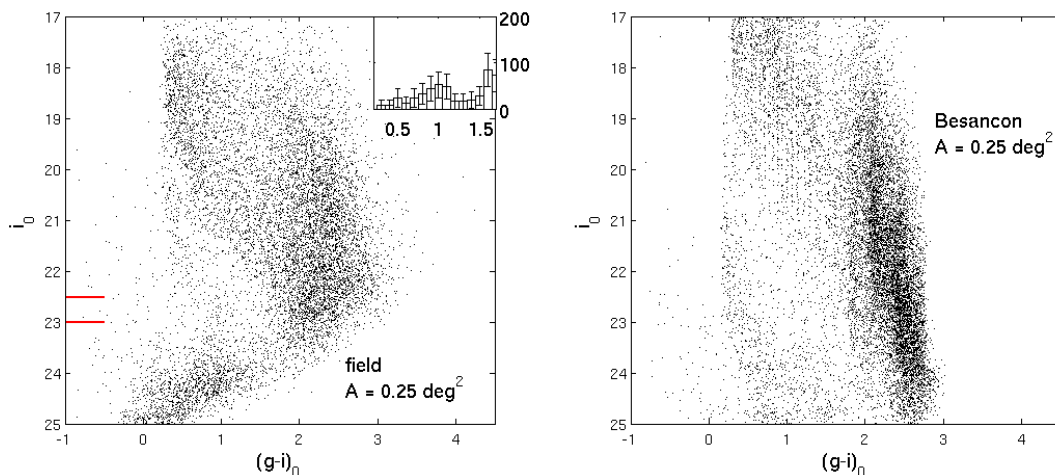


**Figure 3.** The CMDs of contaminant sources. *Left panel:* the CMD of point sources lying in the field selection boxes, scaled to an arbitrary area of  $0.25 \text{ deg}^2$ . The inset shows the colour histogram of sources per unit area with  $(i_{0,TRGB\_NGC185} + 2.0) < i_0 < (i_{0,TRGB\_NGC185} + 2.5)$  (this magnitude range is denoted with red lines on the y-axis). At fainter magnitudes, unresolved galaxies dominate the CMD. *Right panel:* simulated Galactic foreground from the Besançon model, scaled to an area of  $0.25 \text{ deg}^2$ . The simulation has been convolved with photometric errors (as a function of magnitude only) stemming from our photometry, but is not corrected for the data incompleteness.

our contaminant population in subsequent analyses. Finally, for the observed field CMD, we compute the colour histogram of sources that lie within the RGB selection box and have magnitudes in the range  $(i_{0,TRGB\_NGC185} + 2.0) < i_0 < (i_{0,TRGB\_NGC185} + 2.5)$ . The over-density of sources at colours  $(g - i)_0 \sim 1$  results from M31 halo stars, while at redder colours the Galactic foreground dominates.

### 3.2 Colour-magnitude diagrams as a function of radius

To explore how the stellar populations vary across the face of each galaxy, we construct CMDs in four elliptical bins spanning a range of radii and assuming the average  $PAs$  and ellipticities derived in this study (see Sect. 4). For NGC185, we restrict our analysis here and throughout the rest of the paper to  $\leq 0.5 \text{ deg}$  to avoid contamination from NGC147’s tidal tails. The CMDs are shown in Fig. 4 and 5, with and without isochrones overlaid.

In both systems, a clear signature of an RGB population is seen at all radii demonstrating the significant extents of these dwarf galaxies. In addition, the width of the RGB clearly decreases as a function of increasing galactocentric radius, suggestive of a smaller dispersion in metallicity in the outermost regions. To demonstrate this, colour histograms for RGB stars (per unit area) in a narrow range of magnitudes  $((i_{0,TRGB} + 2.0) < i_0 < (i_{0,TRGB} + 2.5))$ , assuming the TRGB of each galaxy) are constructed and shown as insets in Fig. 4 and 5. For NGC185, the width of the histogram distribution decreases from the first to the fourth radial bin, and the peak of the distribution also shifts bluewards. For NGC147, the width decreases from the first two to the second two radial bins, but the peak of the distribution does not significantly change. We note that the innermost radial bin for each galaxy is more incomplete at faint magnitudes, due to stellar crowding in these regions.

## 4 SPATIAL ANALYSES

We analyse the spatial distribution of different stellar populations in the observed CMDs. The top panels of Fig. 6 show the distribution (in standard coordinates, centered on each dE) of point sources

falling within the RGB selection boxes drawn in Fig. 1. The gaps between the CCDs in the MegaCam FoV and the saturated stars are clearly visible. Due to the higher central density of NGC185, the innermost  $\sim 0.03 \text{ deg}$  is mostly unresolved. Even in these point source density maps, one can see the significant larger extent of NGC147 compared to NGC185 and evidence of the tidal tails emanating in the north-west/south-east directions at large radii. These low surface brightness tails extend well beyond the area analysed here and are the focus of a companion paper (Irwin et al., in prep).

To create smoothed density maps, we artificially fill these small gaps and holes through populating them to match source counts in adjacent areas. From the gap-filled distribution, we compute the RGB stellar density per  $\text{arcmin}^2$  and smooth the result with a  $2 \times 2 \text{ arcmin}^2$  grid to produce the contour plots shown in the middle panels of Fig. 6. The density contours of NGC185 are regular over its full extent, while NGC147 presents clear twisting of the isophotes at large radius due to the tidal material.

We use the density distribution of RGB stars to compute the position angle  $PA$  and ellipticity  $\epsilon$  as a function of radius in the two galaxies. For this, we adopt the method described in McLaughlin et al. (1994), which employs the first two moments of the spatial distribution. We begin with a circular aperture and calculate the moments, ellipticity and position angle for the enclosed stars within a given radius, using their formulas (8a), (8b) and (8c). We then iterate the process until convergence, i.e. when the shape of the adopted aperture and that of the underlying stellar distribution are the same. To investigate the possibility of radial variations in the derived quantities, we repeat this procedure for a range of radial annuli in steps of  $0.1 \text{ deg}$ , avoiding the innermost  $\sim 0.1 \text{ deg}$  where crowding limits completeness. The bottom panels of Fig. 6 show the  $PA$  and  $\epsilon$  as a function of radius along the semi-major axis and the resulting ellipses are shown in the middle panels of Fig. 6. As can be seen, the  $PA$  and ellipticity vary only mildly as a function of radius for NGC185 with the ellipticity becoming more pronounced at larger radii. On the other hand, as one progresses outwards in NGC147, the isophotes become rounder and the posi-

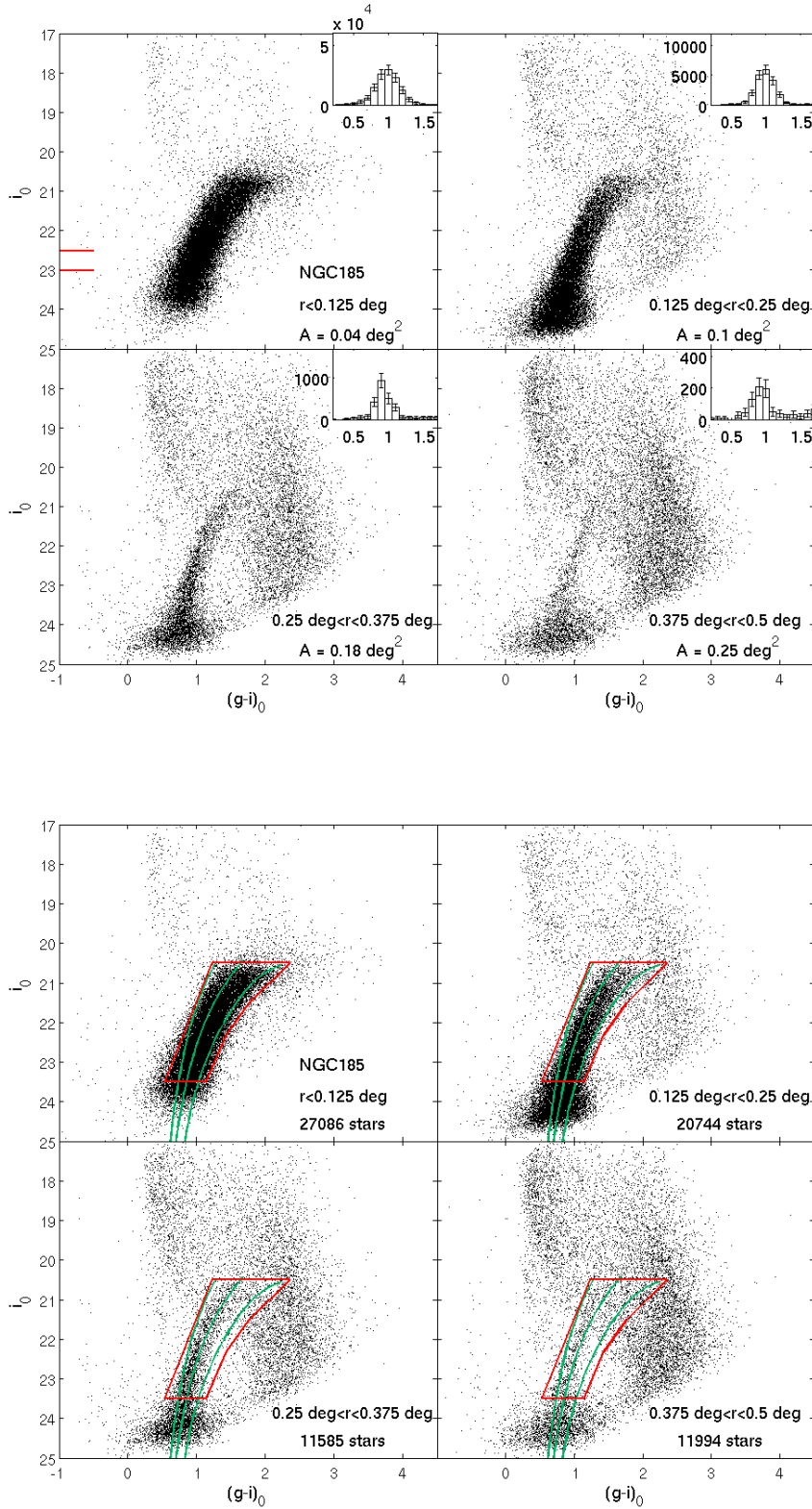


**Figure 4.** CMDs in four radial bins (in 0.125 deg steps) for NGC185, assuming the average *PA* and ellipticity derived in this study. *Upper panels:* The radial limits and enclosed areas are reported in each subpanel. The insets show colour histograms of sources per unit area with  $(i_{0,TRGB\_NGC185} + 2.0) < i_0 < (i_{0,TRGB\_NGC185} + 2.5)$  (this magnitude range is denoted with red lines on the y-axis). *Lower panels:* As above, but with Dartmouth isochrones of fixed age (12 Gyr) and varying metallicity ( $[Fe/H] = -2.5, -1.3$  and  $-0.7$ ) overlaid. Also shown is the adopted RGB selection box and the number of stars per bin.

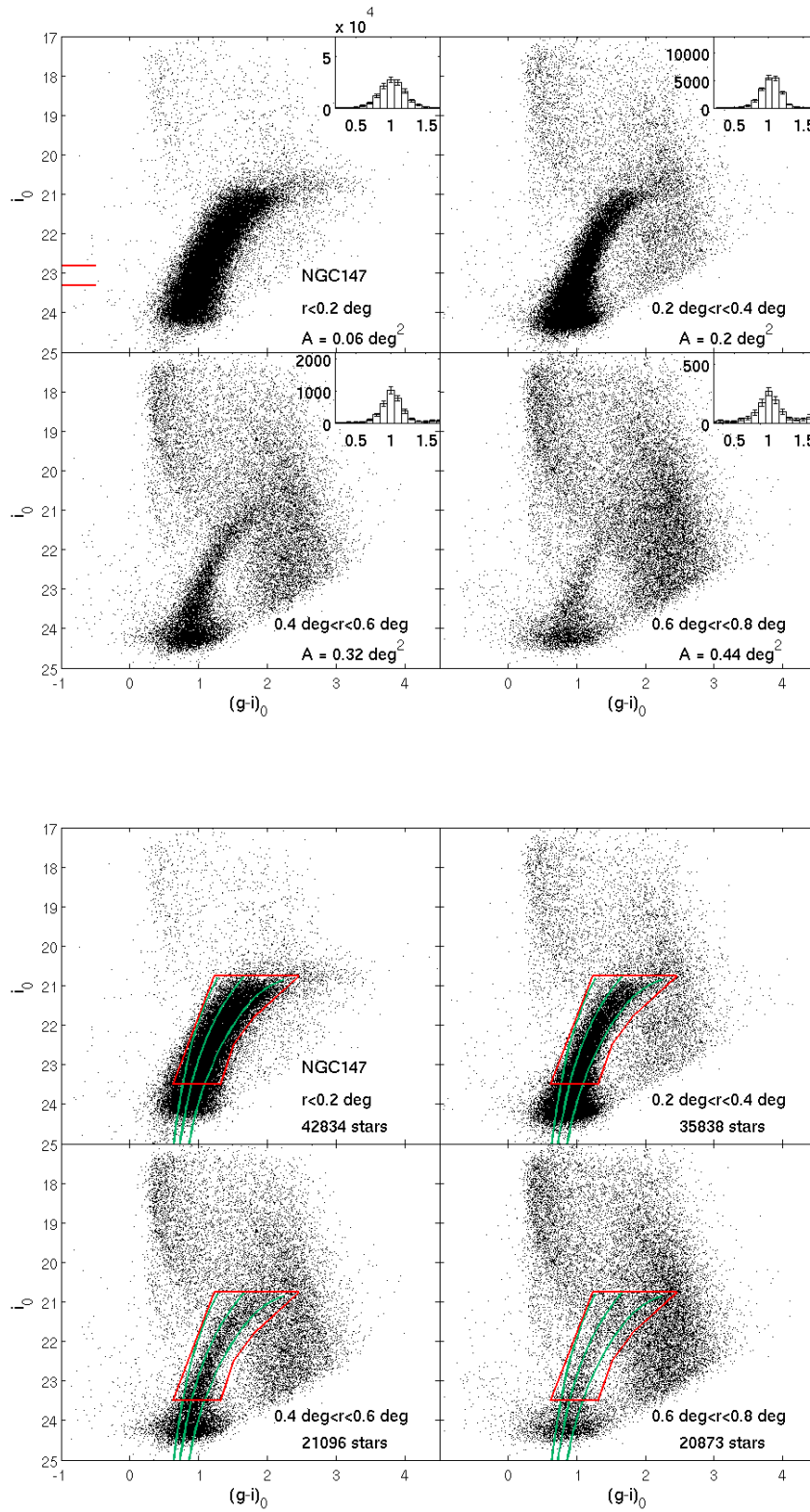


**Figure 5.** Same as Fig. 4, for NGC147 and with radial bins of 0.2 deg width. The insets show colour histograms of sources per unit area with  $(i_{0,TRGB\_NGC147} + 2.0) < i_0 < (i_{0,TRGB\_NGC147} + 2.5)$  (this magnitude range is denoted with red lines on the y-axis).

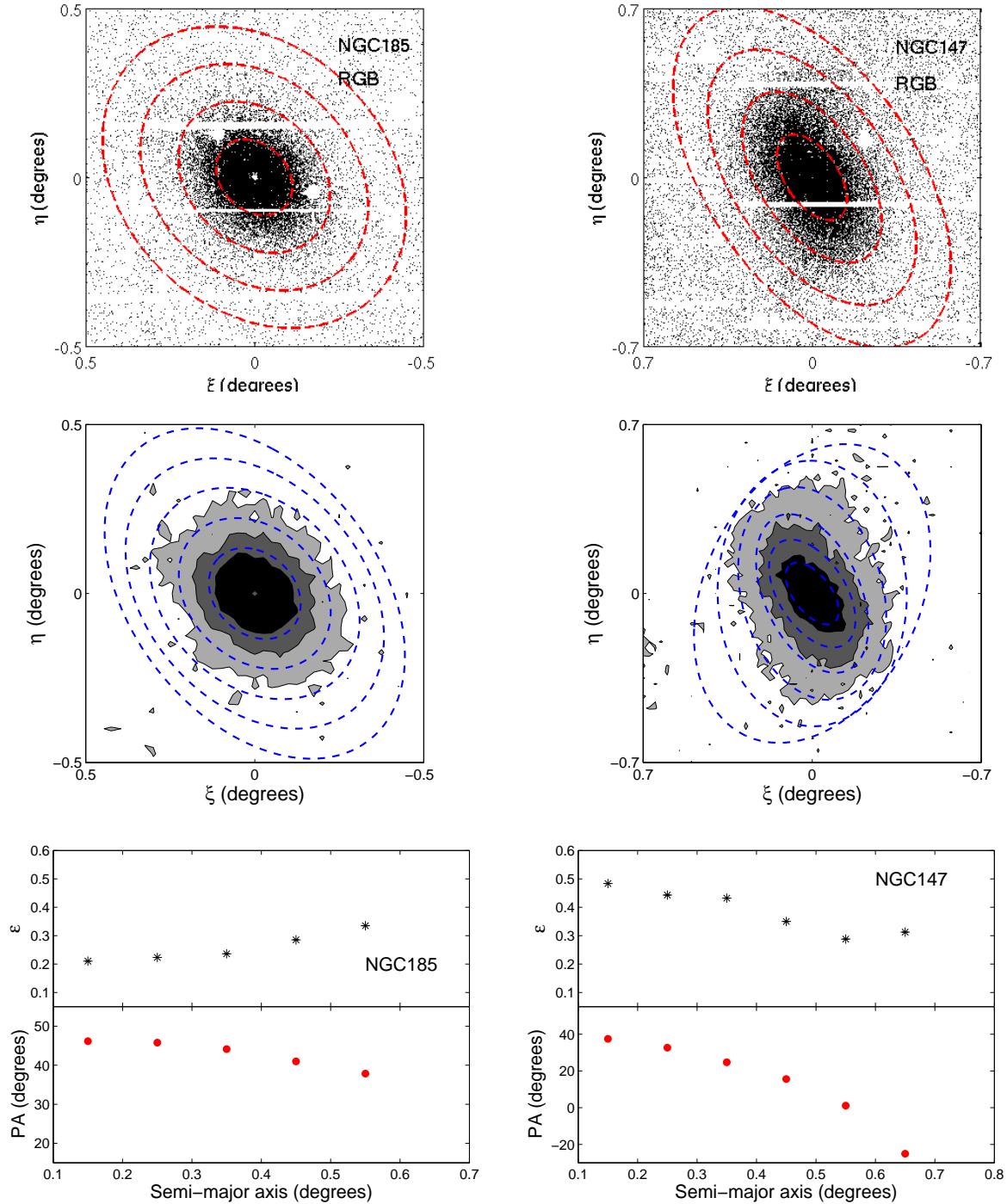


**Figure 6.** *Top panels:* The spatial distribution of RGB stars in standard coordinates for NGC185 (left) and NGC147 (right). White stripes indicate gaps between CCDs and holes stem from saturated stars. We draw ellipses at 0.125, 0.25, 0.375 and 0.5 deg for NGC185 and at 0.2, 0.4, 0.6 and 0.8 deg for NGC147, with average position angle and ellipticity derived in this study, corresponding to the radial bins shown in Fig. 4 and 5. *Middle panels:* RGB density maps. The survey gaps/holes have been filled with artificial stars, and the isodensity contours are logarithmically spaced and indicate densities of  $\sim 4$ , 16 and 64 stars per 1 arcmin<sup>2</sup>. Position angle and ellipticity are recomputed for 0.1 deg radial annuli (blue dashed ellipses). *Bottom panels:* Position angle and ellipticity as a function of distance along the semi-major axis, calculated for annuli centred on each radial point. The errorbars are smaller than the symbols.

tion angle twists strongly, both a direct result of the emergence of the tidal tails.

In the subsequent analysis, we adopt the average  $PA$  and  $\epsilon$  inside 0.5 deg for NGC185 and inside 0.4 deg for NGC147. We obtain  $PA_{NGC185} = 45.9^\circ \pm 1.2$ ,  $\epsilon_{NGC185} = 0.22 \pm 0.01$ , and

$PA_{NGC147} = 34.2^\circ \pm 3.6$ ,  $\epsilon_{NGC147} = 0.46 \pm 0.02$ . These values are in good agreement with  $PA_{NGC185} = 42.9^\circ$ ,  $\epsilon_{NGC185} = 0.23$ , and  $PA_{NGC147} = 28.4^\circ$ ,  $\epsilon_{NGC147} = 0.44$ , reported by Geha et al. (2010), who derived them from the optical photometry of Kent (1987) spanning  $\sim 5'$  and  $7'$  for NGC147 and NGC185, respectively. Ellipses



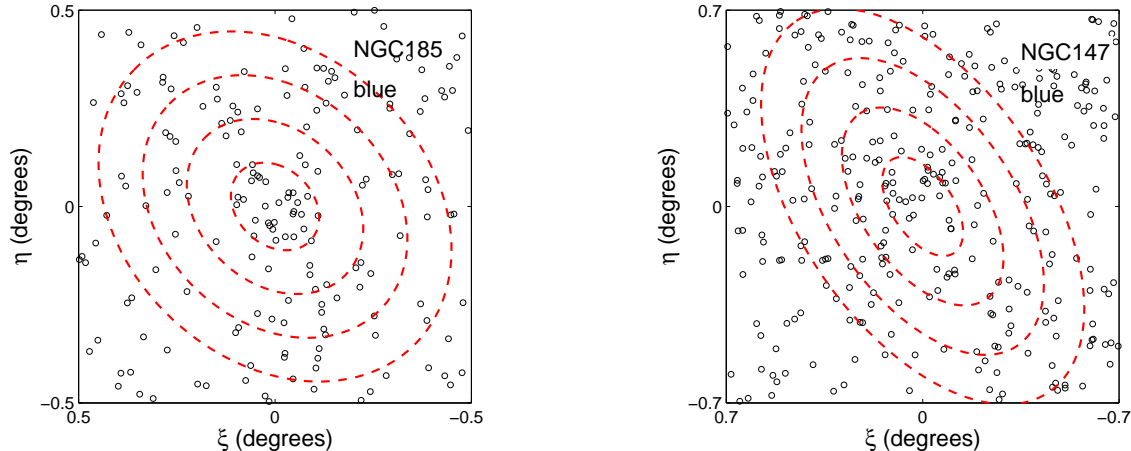


**Figure 7.** Spatial distribution of blue sources, consistent with being candidate MS stars, in each of the target galaxies. Ellipses are as in the top panels of Fig. 6.

corresponding to these parameters are drawn in the top panels of Fig. 6.

We also investigate the spatial distribution of sources with  $(g - i)_0 < 0$  which are candidate young MS populations. Fig. 7 shows a tentative overdensity of such sources in the central region of NGC185, while no obvious enhancement is observed in NGC147. This is consistent with previous studies, as further discussed in Sect. 5.2. Stars falling within the two foreground selection boxes drawn in Fig. 1 are homogeneously distributed, as expected for Milky Way populations. Sources classified as “extended” (and therefore rejected by our quality cuts) are also mostly uniformly distributed but show enhancements in the central regions of both dEs. This suggests that some fraction of genuine RGB stars in these parts are misclassified as extended sources due to blending. We will return to this issue in the next section.

## 5 RADIAL PROFILES

In this section, we derive radial surface brightness profiles for the dEs by combining diffuse light and resolved star counts. While it is challenging to trace diffuse light in faint galactic outskirts, this is the only technique applicable to the central regions, where high stellar crowding hampers the resolution of individual sources (see, e.g., Fig. 6). On the other hand, resolved star counts allow us to trace the light profiles out to the largest galactocentric distances probed by our dataset.

### 5.1 Surface brightness profiles

We exploit the PAndAS images to derive a  $g$ -band surface brightness profile from the diffuse light in the innermost  $10' \times 10'$  of each galaxy. After masking out bright stars, we compute the median of the pixel values in concentric ellipses (with our adopted values of average  $PA$  and  $\epsilon$ ). In order to derive the sky value, we average the mode of the pixel values in two  $\sim 2.5' \times 2.5'$  regions located at  $15'$  on opposite sides of each galaxy, and take the sky uncertainty to be the standard deviation of these values. We convert the resulting profile into mag per arcsec<sup>2</sup>, and de-redden by adopting the median  $E(B - V)$  value within the considered area.

The derived surface brightness profiles are presented in Fig.

8. As pointed out before, the central surface brightness reached in NGC185 is higher than in NGC147 (e.g. Geha et al. 2010, and references therein). For NGC185, we trace the diffuse light profile out  $\sim 0.12$  deg and find a best-fitting Sersic law (Sersic 1968) with  $r_{\text{eff}} = 3.01' \pm 0.01'$  and  $n = 1.80 \pm 0.01$ . The dust lane in the central  $\sim 0.005$  deg<sup>2</sup> of NGC185 does not significantly alter the shape of the  $g$ -band profile with respect to redder bands (see also Kim & Lee 1998). We cross-check this by measuring the average shift between the  $g$ - and  $i$ -band profiles within  $\sim 0.005$  deg<sup>2</sup> for both NGC185 and NGC147. We use the latter as a benchmark given the absence of dust and assume comparable ages and metallicities, and we find the shifts to be consistent within the errorbars. For NGC147, we trace the profile to  $\sim 0.17$  deg, and find  $r_{\text{eff}} = 5.23' \pm 0.03'$  and  $n = 1.36 \pm 0.01$ .

Geha et al. (2010) used the  $r$ -band photometry of Kent (1987) and the assumption of a constant  $B - V$  colour to derive  $V$ -band surface brightness profiles out to radii  $\sim 7'$  and  $5'$  in NGC185 and NGC147, respectively. They find slightly lower values of  $n_{\text{NGC185}} = 1.76$  and  $n_{\text{NGC147}} = 1.04$ . Their Sersic fit is performed with fixed values of effective radius, adopted from De Rijcke et al. (2006). These values are obtained from NIR (2MASS) photometric data in the innermost  $\sim 4'$  of each dE, and are  $r_{\text{eff}} = 1.50'$  for NGC185 and  $r_{\text{eff}} = 2.04'$  for NGC147, thus at least a factor of two smaller than our best-fit values. The factor of two difference holds true when we extend the comparison to previous scale-length estimates resulting from fitting exponential functions or King profiles (Hodge 1963, 1976; Kent 1987; Caldwell et al. 1992; Lee et al. 1993; Kim & Lee 1998).

### 5.2 Number density profiles

To construct accurate star count profiles, we need to account for the contaminant level and its uncertainty. Fig. 9 shows the radial surface density profiles as a function of elliptical radius for RGB stars and blue sources in each galaxy, with the field contamination level and uncertainty indicated. These are calculated as the average and standard deviation of the number densities of objects falling within the RGB and blue selection boxes in our two adopted field regions (Fig. 2).

Contaminants arise from Milky Way foreground stars, M31 halo stars and unresolved background galaxies. While it is rea-

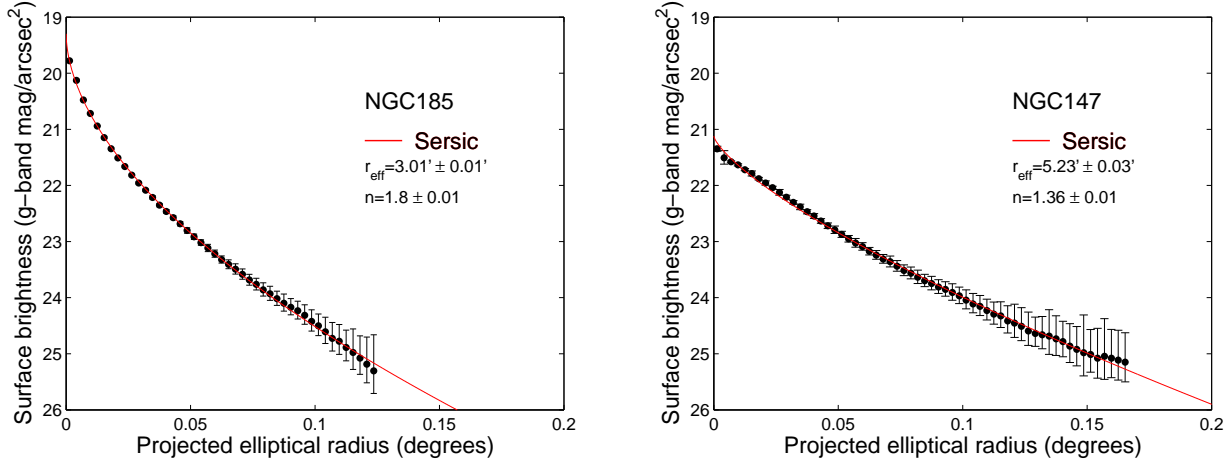


**Figure 8.** Surface brightness profiles (g-band) for NGC185 (left) and NGC147 (right), derived from diffuse light analyses alone. The best-fit Sersic profiles are overlaid, and the respective parameters reported.

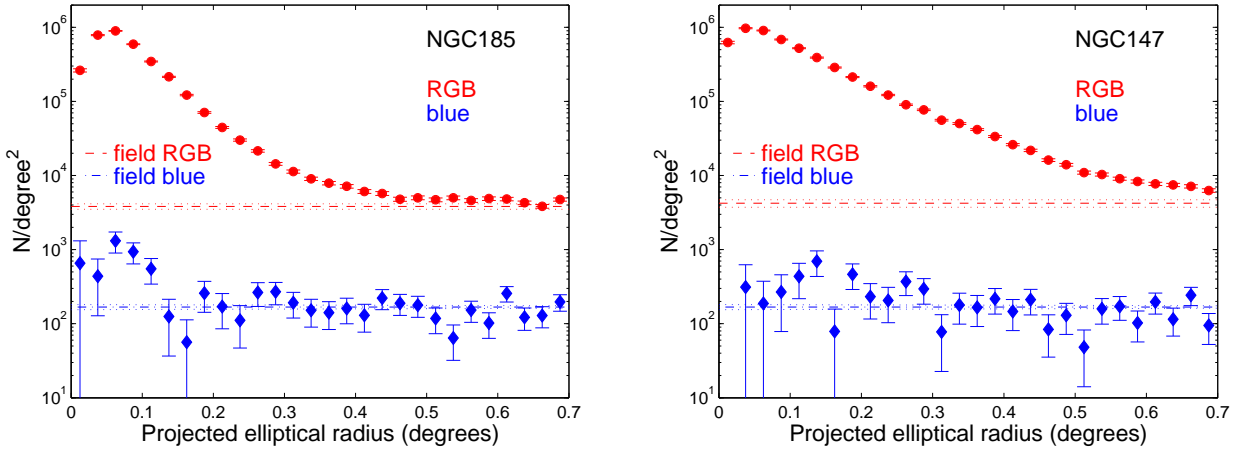


**Figure 9.** Radial star count profiles for NGC185 (left) and NGC147 (right). Red circles are RGB stars, while blue diamonds are blue sources. The error bars are Poissonian. The red dashed line indicates the surface density of sources falling within the RGB box in the adopted field regions, i.e. the contaminant level (see Fig. 2), while red dotted lines indicate the dispersion around this value. The blue dot-dashed line is the contaminant level for sources falling within the blue star selection box.

sonable to expect that unresolved galaxies and M31 halo stars are smoothly distributed across our FoV, the Galactic foreground may vary substantially. To check this, we have inspected the maps of the Milky Way foreground populations within the PAndAS area presented by Martin et al. (2013). Their Fig. 2 reveals that there are no obvious foreground overdensities in the vicinity of NGC185 and NGC147 at magnitudes that would affect our RGB selection box. As a further check, we also use the colour-magnitude contamination model presented in Martin et al. (2013, their formula 12) in order to estimate the foreground number density in our RGB selection box, at the position of the target dEs. The values we obtain from the model are consistent with, but lower by  $\sim 5 - 10\%$  with respect to, our direct estimates. This may be due to the additional sparse M31 halo component, and/or to low-level foreground sub-structure.

The RGB star count profile of NGC185 approaches the contaminant level at  $\geq 0.5$  deg, and then plateaus at a value slightly above this. This is likely due to low-level contamination from

NGC147’s tidal tails which start to contribute in these parts. On the other hand, the RGB profile of NGC147 declines smoothly and remains well above the field level out to 0.7 deg. Fig. 10 examines how the contaminant-subtracted RGB star count profiles vary as a function of azimuthal angle. Each galaxy is split into eight  $45^\circ$ -wide wedges, with the central angle of each wedge measured clockwise from the north-eastern semi-major axis. For NGC185, this analysis reveals no significant change in the radial profiles as a function of azimuthal angle. For NGC147, there is a clear excess of stars at large radius in the directions of  $45^\circ - 90^\circ$  and  $225^\circ - 270^\circ$ , consistent with the presence of the tidal tails (see Fig. 6). It can be seen that the excess stars in these directions is what causes the azimuthally-averaged radial density profile to remain above the field level out to 0.7 deg. In directions away from the tidal tails, the RGB star count profile falls off more steeply at large radius, and reaches the background level at  $\sim 0.5$  deg. Note that the RGB density profiles in all cases show a drop in number counts at small radii ( $\lesssim 0.05$  deg), due to incompleteness in these parts.

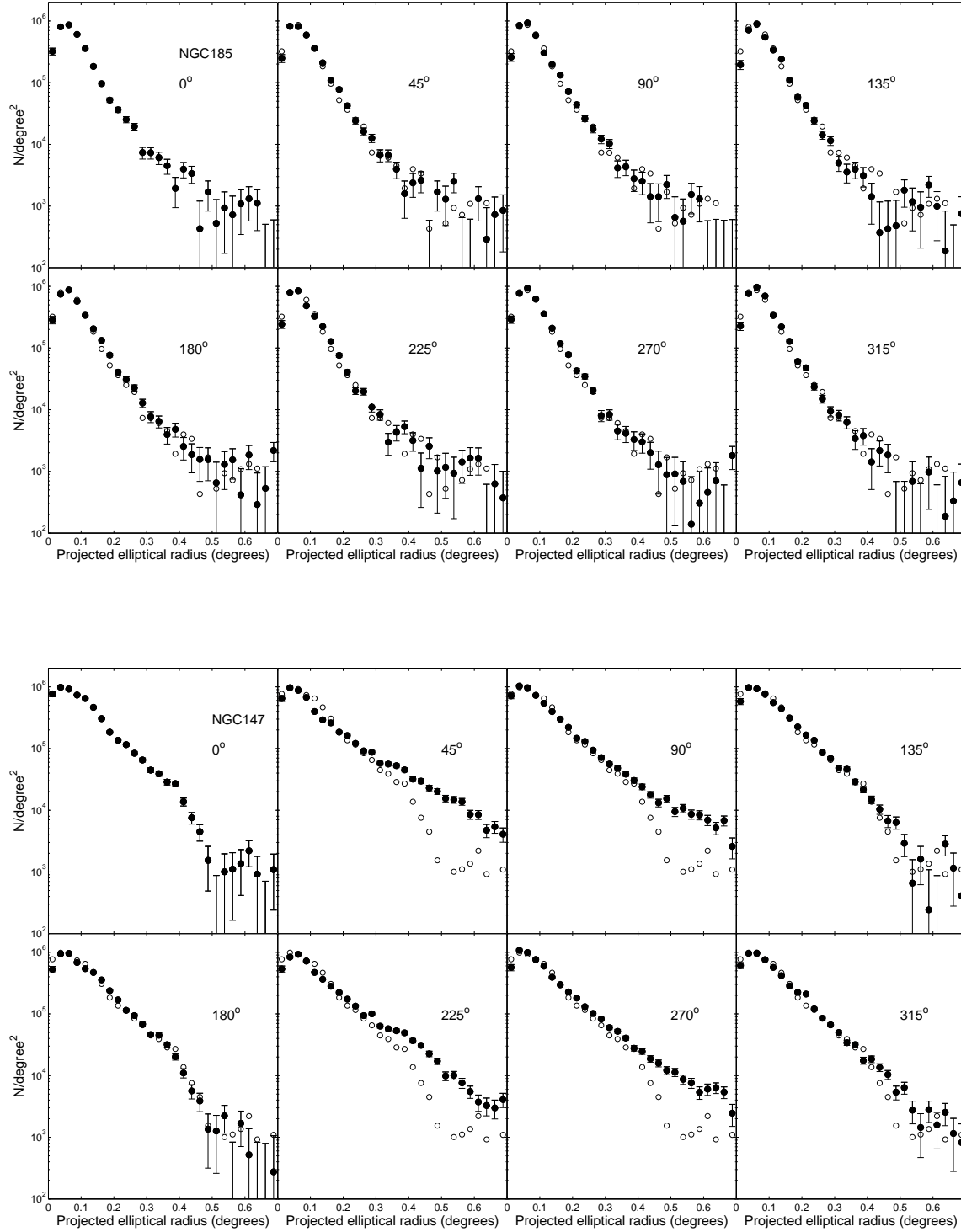


**Figure 10.** Radial star count profiles of RGB stars in  $45^\circ$  wedges as a function of azimuthal angle, for both galaxies. The average  $PA$  and ellipticity derived in this study are assumed, and the profiles have been contaminant-subtracted. The central angle of each wedge is measured clockwise from the north-eastern semi-major axis and is reported in each sub-panel. The error bars are Poissonian. The  $\theta = 0^\circ$  profile is repeated in all other panels for reference (open symbols).

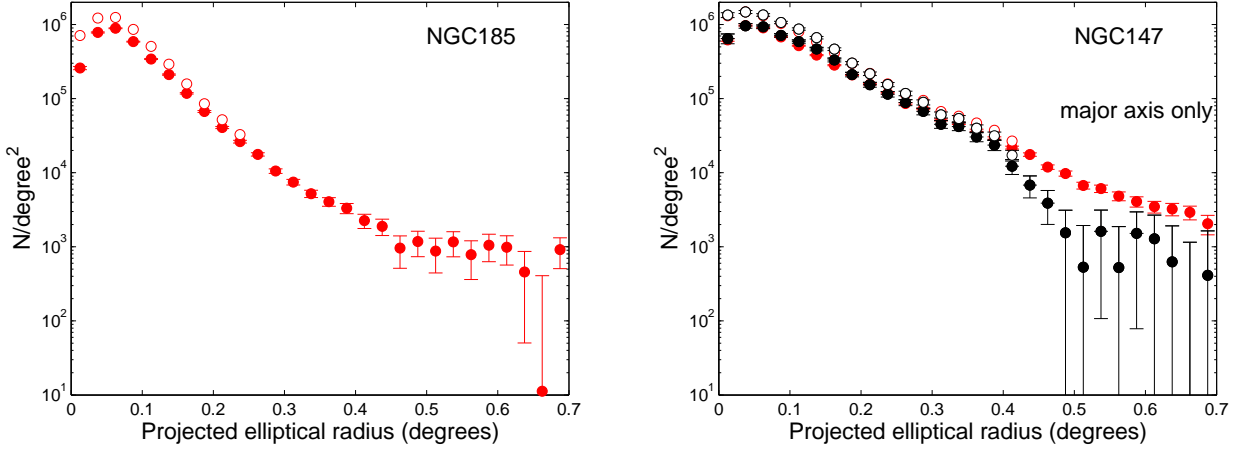


**Figure 11.** Contaminant-subtracted RGB star count profiles for NGC185 (left) and NGC147 (right). Red filled circles show RGB stars only, while open red circles indicate the sum of both stars and extended sources within the RGB selection boxes. For NGC147, black symbols are the same as above, but for the major axis directions only (i.e., the azimuthal wedges centered on  $0^\circ$  and  $180^\circ$  from Fig. 9), to avoid the extended tidal tails. Error bars are Poissonian and include the field level uncertainties.

The radial surface density profile of blue sources is also shown in Fig. 9. A mild central excess ( $\geq 2\sigma$ ) can be seen in NGC185. While the presence of young stars is well known in NGC185, previous observations have indicated they are mostly confined to the inner  $\sim 0.03$  deg (Martínez-Delgado et al. 1999). Our observations suggest this young component may be more distributed, consistent with inferences from some other studies (e.g. Butler & Martínez-Delgado 2005; Marleau et al. 2010). While NGC147 shows a marginal overdensity of blue sources in its central regions, this is probably not significant given the uncertainties. In both systems, the high central densities lead to incompleteness in the very innermost ( $< 0.05$  deg) regions, leading to the turnover of the profiles.

In Fig. 11, we show the contaminant-subtracted surface density profile constructed using only point sources (filled symbols) as well as point sources plus extended sources (open symbols), which fall within the RGB selection box. In the latter case, we only add extended sources in when their surface density exceeds that of the background by  $> 5\sigma$ , corresponding to a region inside 0.25 deg for NGC185 and 0.4 deg for NGC147. The motivation for including these sources is to account for stars that have been misclassified as extended due to the severe crowding and blending at small radii. Even after the inclusion of these sources, the innermost regions are still incompleteness-limited and hence we must resort to using diffuse light in these parts. The star count profile of NGC185 can be reliably traced out to a radius of  $\sim 0.45$  deg, corresponding to  $\sim 5$  kpc. For NGC147, we show the azimuthally-averaged star count profile as well as the profile along the major axis only, calculated as the average of the azimuthal profiles in centered on  $0^\circ$  and  $180^\circ$  (Fig. 10). After field level subtraction, the major axis profile, which is virtually free from contamination by the tidal tails, extends to  $\sim 0.5$  deg, or  $\sim 5$  kpc at NGC147’s distance. A steep break is present in the profile at large radius, most likely due to the ongoing tidal disruption.

### 5.3 Combined profiles

We combine the diffuse light profiles shown in Fig. 8 with the star count profiles  $\Sigma(r)$  in order to trace the surface brightness variation

over a large radial extent. To do this, we use the relation  $\mu(r) = -2.5 \log_{10}(\Sigma(r)) + ZP$ , where the zeropoint  $ZP$  is derived from the overlapping region between the profiles (i.e.,  $r \sim 0.1 - 0.13$  deg for NGC185 and  $r \sim 0.1 - 0.15$  deg for NGC147). We obtain  $ZP = 21.37$  for NGC185 and  $ZP = 21.36$  for NGC147. In constructing these profiles, we use the azimuthally-averaged star count profiles for both dEs. Fig. 12 demonstrates the advantage of this technique, allowing us to trace the surface brightness from  $\mu_g \sim 20 - 22$  mag arcsec $^{-2}$  in the central regions to  $\sim 32 - 33$  mag arcsec $^{-2}$  at the largest radii.

We fit Sersic models to the composite profiles and report the results in Tab. 2. While our earlier analysis of the diffuse light was limited to radii within  $\lesssim 0.2$  deg, we can fit the composite profile out to roughly twice that radius. In particular, we fit NGC185 in the range of  $0 - 0.45$  deg and NGC147 in the range  $0 - 0.4$  deg, the latter chosen to avoid the tidal tails. For NGC185, the values obtained from the diffuse light and composite profiles are consistent with each other indicating that there is no strong change in the profile shape out to this radius. Beyond 0.45 deg, there is an excess of light compared to the extrapolation of the fit, but this is likely due to contamination of these regions by NGC147’s tidal tails, as mentioned previously. For NGC147, both  $n$  and  $r_{\text{eff}}$  derived from the composite profile fit are higher than the diffuse light-only estimates, suggesting the surface brightness profile might flatten somewhat beyond the inner regions. Additionally, the fit seems to provide a good description of the surface brightness profile even beyond the radial range of the fit.

The only other studies to probe relatively large galactocentric radii in NGC185 and NGC147 are Battinelli & Demers (2004b,a), who analyse the distribution of giant stars in both dEs out to a radius of  $\sim 0.3$  deg. The scale-lengths  $\alpha$  they obtain from exponential fits can be converted to effective (half-light) radii as  $r_{\text{eff}} \sim 1.668\alpha$ , returning  $r_{\text{eff}} = 4.2' \pm 0.1'$  for NGC185 and  $r_{\text{eff}} = 6.8' \pm 0.2'$  for NGC147. These values can be compared to those reported in Tab. 2. The effective radius for NGC185 computed by Battinelli & Demers (2004b) is larger than ours, possibly due to the fact that they adopt slightly larger  $PA$  and  $\epsilon$  values; the radius for NGC147 from Battinelli & Demers (2004a) is consistent with ours.

We derive total magnitudes by integrating our Sersic com-

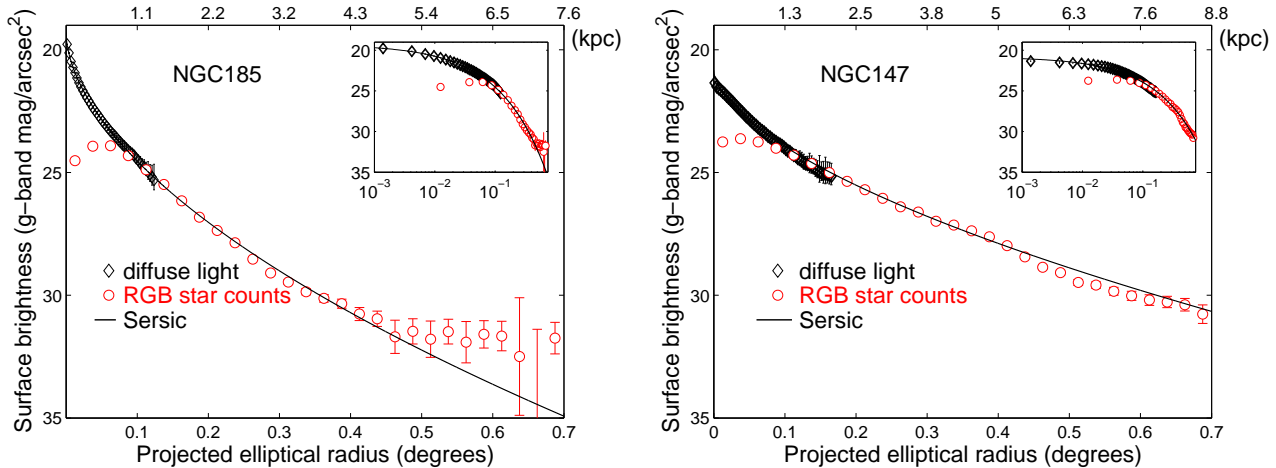


**Figure 12.** Composite surface brightness profiles for NGC185 (left) and NGC147 (right) derived from merging diffuse light profiles (black open diamonds) with star count profiles (open red circles). The best-fitting functions to the global profiles are overlaid; the insets show the profiles on a logarithmic scale. The upper axis gives the radius in physical units.

**Table 2.** Best-fitting Sersic parameters to the composite profiles.

	NGC185	NGC147
$\mu_{g,\text{eff}}$ (mag)	$22.81 \pm 0.03$	$24.15 \pm 0.03$
$r_{\text{eff}}$ (′)	$2.94 \pm 0.04$	$6.70 \pm 0.09$
$r_{\text{eff}}$ (kpc)	$0.53 \pm 0.01$	$1.41 \pm 0.02$
$n$	$1.78 \pm 0.02$	$1.69 \pm 0.03$
$\chi^2_{\text{red}}$	0.16	0.13
$M_V$ (mag)	$-15.5 \pm 0.04$	$-16.5 \pm 0.04$

posite profiles to infinity and obtain  $M_g = -15.36 \pm 0.04$  for NGC185 and  $M_g = -16.36 \pm 0.04$  for NGC147. Adopting the mean RGB color of the two dEs ( $(g - i)_0 \sim 1.2$ ), we use the conversion reported in Sect. 4 of Veljanoski et al. (2013) to transform the CFHT/MegaCam bands into Johnson/Cousins, and obtain  $M_V \sim -15.5$  for NGC185 and  $M_V \sim -16.5$  for NGC147. While the previously-reported literature magnitudes for these systems are similar (see Tab. 1), our revised values based on new profile fits indicate that NGC147 is significantly more luminous than NGC185, arising from the significant luminosity contained in its wings.

## 6 METALLICITY DISTRIBUTION FUNCTIONS

The mean locus and width of the RGB are widely used as indicators of the metal content of a galaxy, given that they are more sensitive to metallicity than to age (e.g. VandenBerg et al. 2006). If it is assumed that RGB stars are coeval, the width of the RGB can be interpreted as the spread in metallicity within a galaxy. We adopt the updated 2012 version of the Dartmouth stellar isochrones (Dotter et al. 2008; McConnachie et al. 2010) with a fixed age of 12 Gyr and  $[\alpha/\text{Fe}] = +0.0$  to derive the photometric MDFs for each galaxy. We only consider RGB stars bounded by the  $[\text{Fe}/\text{H}] = -2.5$  and  $-0.3$  isochrones, with magnitudes  $i_0 < 23$  and fainter than the TRGB. Metallicities are computed by linearly interpolating between isochrones with a  $[\text{Fe}/\text{H}]$  spacing of 0.2 dex.

The influence of contaminants again needs to be taken into account when interpreting the MDFs. To assess this, we construct MDFs for point sources in the adopted field regions that fulfill the

same colour-magnitude selection criteria as used for RGB stars in the dwarf galaxies. As before, it is reasonable to assume that these sources are not genuine RGB stars but foreground/background contaminants. We subtract the contaminant MDFs (after area scaling) from the MDFs of the target galaxies and fit a Gaussian to quantify the mean metallicity and dispersion. For NGC185, we find  $\langle [\text{Fe}/\text{H}] \rangle = -1.08$  and  $\sigma_{[\text{Fe}/\text{H}]} = 0.39$  (within 0.5 deg), while for NGC147 we find  $\langle [\text{Fe}/\text{H}] \rangle = -0.96$  and  $\sigma_{[\text{Fe}/\text{H}]} = 0.30$  (within 0.8 deg). These global estimates may be underestimates of the true values since the RGB sample is incomplete at small radii, where the most metal-rich stars are likely to lie.

The MDFs as a function of radius are presented in Fig. 13, using the same radial bins as in Fig. 4 and 5. We do not consider the innermost bin due to incompleteness. In the same figure, we report the mean metallicity and metallicity dispersion obtained from the best-fitting Gaussian (red lines) in each bin. The uncertainty in the individual RGB metallicity values is much smaller than the derived metallicity dispersion. We do not include the rejected extended sources in computing the MDFs as they comprise only a small fraction of the total source counts in the radial bins considered.

The two dEs show very different radial trends in their MDFs. The mean metallicity in NGC 185 decreases significantly as a function of radius and presents a gradient of  $\Delta \frac{\langle [\text{Fe}/\text{H}] \rangle}{R} \sim -0.15$  dex/kpc over radii spanning 0.125 to 0.5 deg. In terms of physical radii, this corresponds to  $\sim 1.3$ –5.4 kpc, or  $\sim 4$ –9  $r_{\text{eff}}$ . The global metallicity for NGC 185 found above ( $\langle [\text{Fe}/\text{H}] \rangle = -1.08$ ) is higher than in any of the panels shown in Fig. 13, indicating that this gradient extends to stars inside 0.125 deg. The width of the MDF becomes slightly narrower beyond 0.375 deg, varying from  $\sigma_{[\text{Fe}/\text{H}]} = 0.35$  to 0.28. On the other hand, the mean metallicity varies only slightly across NGC147, amounting to a gradient of  $\Delta \frac{\langle [\text{Fe}/\text{H}] \rangle}{R} \sim -0.02$  dex/kpc from 0.2 to 0.6 deg. This corresponds to  $\sim 2.5$ –6.3 kpc, or  $\sim 2.5$ –4.5  $r_{\text{eff}}$ . In the outermost bin, stars from the tidal tails contribute (see Fig. 11) but their stellar density is low and comparable to the contaminant count. The peak in the MDF at  $\sim -0.4$  dex probably arises from residual contaminants as it corresponds to a similar peak seen in the field MDF (see inset). If we make the extreme assumption that all stars with  $[\text{Fe}/\text{H}] > -0.7$  in our outermost bin

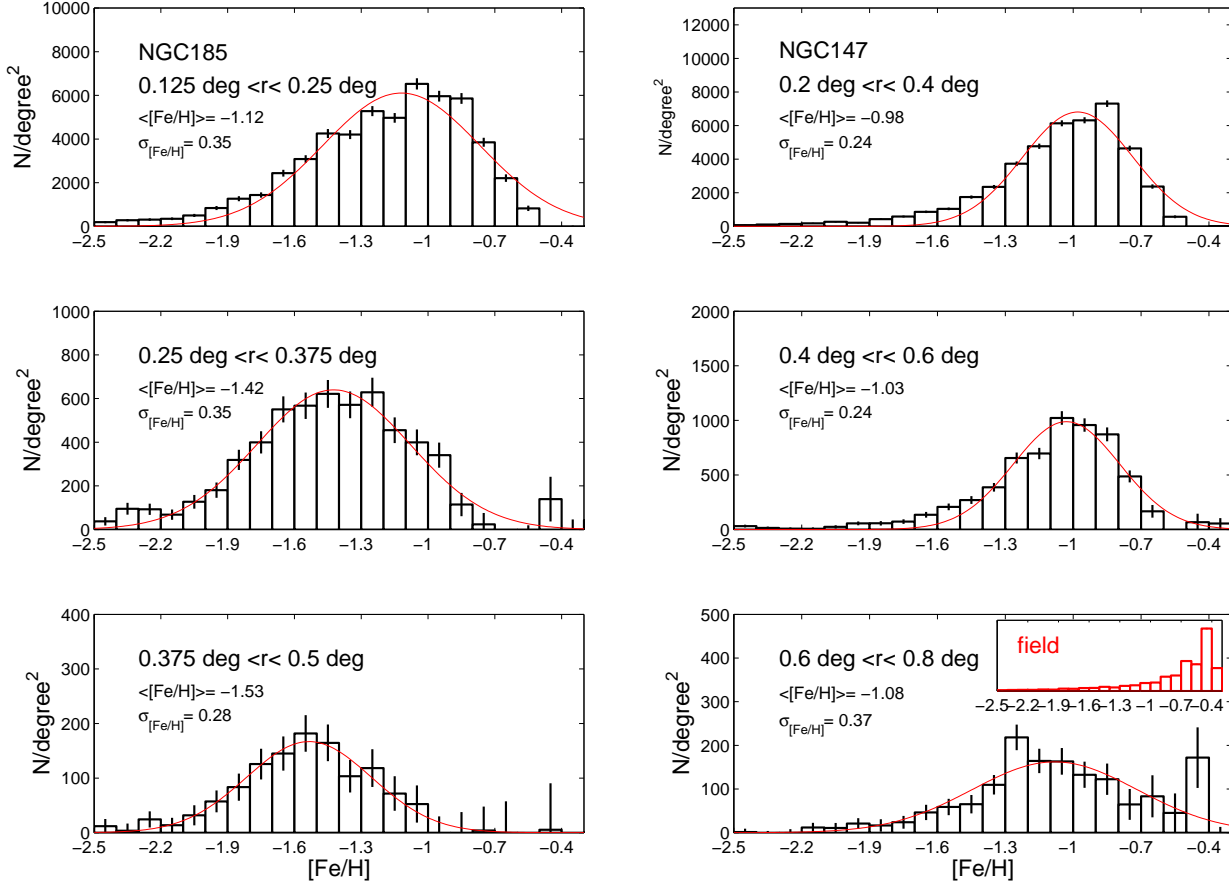


**Figure 13.** Photometric MDFs (per unit area) as a function of radius for NGC 185 (left) and NGC 147 (right), derived via isochrone interpolation assuming a fixed age (12 Gyr). We only consider RGB stars with  $i_{0,TRGB} < i_0 < 23$ . The field contamination has been subtracted (see text for details). The radial bin, mean metallicity and metallicity dispersion (obtained from the best-fitting Gaussian, red curve) are reported for each sub-panel. The errorbars are Poissonian.

are contaminants, the best-fitting mean metallicity and metallicity spread change to  $\langle [Fe/H] \rangle = -1.13 \pm 0.28$ .

Photometric metallicity estimates can suffer from uncertainties due to the underlying assumptions (i.e., a coeval old population) and due to the choice of theoretical libraries. While this limits their ability to return precise *absolute* values, the derivation of *relative* values, e.g. radial trends, should be robust. We consider the possible biases stemming from the neglect of intermediate-age populations, which are known to be present in the target dEs (e.g. Nowotny et al. 2003; Battinelli & Demers 2004b,a; Butler & Martínez-Delgado 2005; Davidge 2005; Kang et al. 2005, see also our Fig. 1). Both intermediate-age RGB and old first-ascent AGB stars will populate the blue side of the RGB ( $[Fe/H] \lesssim -1.0$  dex) and thus will artificially increase the metal-poor fraction in the observed MDFs. If these populations are more centrally concentrated than the bulk of the old populations in these galaxies, as may be the case (Battinelli & Demers 2004b,a), they will also skew photometric metallicity gradients. Their number counts thus mainly affect the MDFs at small radii ( $< 0.125$  deg for NGC185 and  $< 0.4$  deg for NGC147). If we assume, for example, that 20% (50%) of the stars blueward of  $[Fe/H] \sim -1.0$  dex are intermediate-age RGB stars, we obtain best-fitting values for

the innermost radial bin of  $\langle [Fe/H] \rangle = -1.08$  ( $-0.96$ ) for NGC185 and  $\langle [Fe/H] \rangle = -0.95$  ( $-0.89$ ) for NGC147. These values are more metal-rich than the original values by  $\sim 0.04$  dex ( $\sim 0.16$  dex) for NGC185, and  $\sim 0.03$  dex ( $\sim 0.09$  dex) for NGC147, thus not significantly affecting our conclusions about the difference in metallicity gradient between the two galaxies.

## 7 DISCUSSION

Our wide FoV observations have allowed us to survey the outer regions of NGC185 and NGC147, well beyond previous studies, and establish that the stellar extents of these systems are greater than the literature estimates. Until our work, the widest FoV CCD observations of these dEs have been performed by Battinelli & Demers (2004b,a), covering  $42' \times 28'$  centered on each galaxy with a limiting magnitude of  $\sim 2$  mag below the TRGB in the *I* band. The spectroscopic samples of Geha et al. (2010) and Ho et al. (2014) reach  $\sim 15'$  on each side of the major axis. Our analysis maps the brightest  $\sim 3$  mag of the RGB over a region of  $\geq 1$  deg<sup>2</sup> around the target galaxies. After correcting for contaminants, we have shown that NGC185's population of RGB stars can be mapped out to at

least 0.5 deg (or  $\sim 5$  kpc). In directions which avoid the tidal tails (i.e., along the major axis), NGC147 can be mapped out to a similar radius. The results of fitting Sersic models to both the diffuse light-only profiles and the composite profiles yield effective radii significantly larger than most previous literature estimates by a factor of  $\sim 2$ , and reveal NGC147 has significant luminosity in its extended wings. We argue that the larger effective radius and shallower surface brightness profile of NGC147 with respect to NGC185 are a result of its strong tidal interaction, and at this stage it is not possible to trace its originally undisturbed profile.

We find that stars in the outskirts of NGC 147 are distributed in a highly asymmetric fashion, with prominent tidal tails elongating in the north/north-west to south/south-east direction. This is in stark contrast to the regular isophotes which characterise the outer regions of NGC185. We cannot rule out the possibility that NGC185 has tidal tails which lie below the surface brightness sensitivity of the PAndAS survey. Tidal effects only become evident at radii where the local crossing time is longer than the time elapsed since a tidal interaction (Peñarrubia et al. 2009), and thus signs of the interaction are erased quicker in the inner regions of a galaxy. The tails in NGC147 become visible at a radius of  $\sim 5$  kpc and at a surface brightness of  $\sim 27.5$  mag arcsec $^{-2}$ . The velocity dispersion of NGC147 is  $\sim 1.5$  higher than that of NGC185 (Geha et al. 2010), thus we would expect to detect possible tails in NGC185 at  $\sim 7.5$  kpc. Within this galactocentric distance we do not observe azimuthal variations in its radial profile (Fig. 10), and if tails were present beyond this radius they would be consistent with the field level at a surface brightness of  $\sim 32$  mag arcsec $^{-2}$ . We conclude that, if a tidal distortion is present in NGC185, it would be significantly weaker than what observed in NGC147.

These different outer structures may hold clues about the interaction histories of the galaxies. Some recent work has suggested that the two dEs do not form a bound pair based on their phase-space distribution functions together with the timing argument (Watkins et al. 2013) or on gravitational arguments (Evslin 2014). Comparing to cosmological simulations, Teyssier et al. (2012) argue that for NGC185 a past passage through the Milky Way is probable. On the other hand, Fattahi et al. (2013) suggest they could be a physical pair based on their proximity, similar luminosities and radial velocities. With the updated values of radial velocities and total mass from Geha et al. (2010) and the distances from Conn et al. (2012), we find the ratio between potential energy and kinetic energy in this system to be  $\sim 1$ , thus the extant data cannot give a conclusive result on whether the two dEs are bound to each other. Any model for the orbital evolution of the two galaxies needs to explain why prominent tidal tails are visible around NGC147 and not NGC185. A possible scenario is one where the two dwarfs were bound to each other in the past and, at their last pericentric passage around M31, NGC147 was closer to M31 than NGC185 was. A separation between the dEs of a few tens of kpc could result in only NGC147 experiencing a strong tidal interaction with M31, as demonstrated by the simulations of Arias et al., submitted.

Geha et al. (2010) derived spectroscopic values for individual RGB stars along the major axis out to 0.25 deg for both galaxies, and more recently Ho et al. (2014) re-analysed the same sample with updated spectroscopic calibrations to derive MDFs and radial metallicity gradients. Our global metallicity and metallicity dispersion for NGC185, dominated by stars in the innermost  $\sim 0.2$  deg, are only slightly lower than the values reported by Ho et al. (2014) and can likely be explained by incompleteness in our star count data at small radii. This is reassuring when considering the uncertainties involved in our photometric method. On the other hand, Ho et al.

(2014) find that the mean metallicity for NGC147 is about twice the value derived by Geha et al. (2010), while our value agrees with the latter. Ho et al. (2014) argue that the higher value found in their more recent analysis would be consistent with the fact that NGC147 has experienced considerable prolonged star formation. Considering metallicity gradients, Battinelli & Demers (2004a) do not find a gradient for NGC185 from the ratio of C- to M-stars, while Battinelli & Demers (2004b) find that for NGC147 [Fe/H] decreases by  $\sim 0.4$  dex within the innermost  $\sim 0.25$  deg. On the other hand, Ho et al. (2014) find a strong metallicity gradient for NGC185 and none for NGC147. This latter result is in line with our results and we have been able to show that these trends continue to larger radii than previously considered.

Metallicity gradients have often been used in the past to constrain the origin of dE galaxies (e.g. Koleva et al. 2009, 2011; Spolaor et al. 2009). The formation of metallicity gradients in isolated dwarf galaxies is generally understood to be a physical process driven by internal feedback and by the stellar orbital anisotropy (Marcolini et al. 2008; Valcke et al. 2008; Revaz et al. 2009; Stinson et al. 2009; Pasetto et al. 2011), but their longevity can critically depend on the galaxy's evolutionary history. The rotating dwarfs simulated in Schroyen et al. (2011) display shallow gradients, while Schroyen et al. (2013) find that non-rotating dwarf galaxies can easily retain their gradients over many Gyr. Ram-pressure stripping and tidal interactions may also play a role in the evolution of dwarf galaxies, especially in transforming a dIrr into a dE (e.g. Moore et al. 1998; Mayer et al. 2006), however models to date have not explored the consequences of these processes for metallicity gradients. Geha et al. (2010)'s analysis shows NGC147 and NGC185 continually rising rotation curves out to at least 0.25 deg. The ratio between the maximum rotation velocity and the velocity dispersion  $V_{max}/\sigma$  for the two dEs is similar ( $\geq 0.9$  for NGC147 and  $\geq 0.65$  for NGC185), and yet we find that they have completely different metallicity gradients. Leaman et al. (2013) compared dE and dIrr dwarfs within the LG, and suggested a correlation between  $V_{max}/\sigma$  and metallicity gradient strength, with lower  $V_{max}/\sigma$  corresponding to steeper gradients. Although this trend agrees with the simulations of Schroyen et al. (2011) (but see Ho et al. 2014), it is at odds with the properties of the dwarfs studied here. The likely reason for this is the strong tidal disruption that NGC147 is experiencing and the rearrangement of material resulting from this.

## 8 CONCLUSIONS

We have performed a deep wide-field analysis of the resolved stellar populations in the dE companions of M31, NGC185 and NGC147. Using data from the PAndAS survey, we have constructed CMDs which reach down to  $\sim 3$  mag below the TRGB and allow us to conduct the first detailed exploration of the structure and stellar content of the peripheral regions of these systems.

Our results can be summarized as follows:

- RGB star count maps of NGC185 exhibit regular, elliptical isophotes out to the furthestmost radii probed, while NGC147 shows prominent isophotal twisting and the emergence of extended tidal tails (see also Irwin et al., in prep.);
- we derive composite surface brightness profiles by combining diffuse light in the central regions of the dEs with resolved stellar counts in the outskirts, enabling us to trace them to magnitudes as faint as  $\mu_g \sim 32$  mag arcsec $^{-2}$ . The profiles of both galaxies can be fit by single Sersic profiles: NGC185 shows a much steeper profile

with a higher central surface brightness with respect to NGC147. Surprisingly, the effective radii we derive are a factor of  $\sim 2$  larger than most previous literature estimates based on smaller FoVs. We use our new profiles to recalculate the integrated magnitudes of the two dEs, concluding both are more luminous than previously recognised and that NGC147 is roughly a magnitude brighter than NGC185;

- we derive photometric metallicity distribution functions for the RGB stars. An analysis of the radial variation in  $[\text{Fe}/\text{H}]$  reveals a pronounced negative gradient in NGC185 ( $\sim -0.15$  dex/kpc in the range  $0.125 < r < 0.5$  deg, or over 2.7 kpc) as opposed to NGC147, which shows a relatively flat metallicity profile ( $\sim -0.02$  dex/kpc in the range  $0.2 < r < 0.6$  deg, or over 2.5 kpc).

The strong evidence of tidal disruption in NGC147 suggests that these two dEs have experienced markedly different evolutionary histories. NGC147 shows a shallower surface brightness profile and metallicity gradient than NGC185, which is likely to result from environmental effects, rather than internal evolution (e.g., rotation). Our observations will be crucial for constraining models of the past histories of these closest dEs.

#### ACKNOWLEDGMENTS

The authors thank the PAndAS collaboration and the referee for useful comments. DC, AMNF and EJB acknowledge support from an STFC Consolidated Grant. DC wishes to kindly thank the hospitality of the Mullard Space Science Laboratory, University College of London, where part of this work has been carried out. Based on observations obtained with MegaPrime/MegaCam, a joint project of CFHT and CEA/DAPNIA, at the Canada-France-Hawaii Telescope (CFHT) which is operated by the National Research Council (NRC) of Canada, the Institut National des Sciences de l'Univers of the Centre National de la Recherche Scientifique of France and the University of Hawaii. This research made use of SAOImage DS9, developed by Smithsonian Astrophysical Observatory, and of the NASA/IPAC Extragalactic Database (NED), which is operated by the Jet Propulsion Laboratory, California Institute of Technology, under contract with the National Aeronautics and Space Administration.

#### REFERENCES

- Baade W., 1944, *ApJ*, 100, 147  
 Barker M. K., Ferguson A. M. N., Irwin M. J., Arimoto N., Jablonka P., 2012, *MNRAS*, 419, 1489  
 Battinelli P., Demers S., 2004a, *A&A*, 418, 33  
 Battinelli P., Demers S., 2004b, *A&A*, 417, 479  
 Bender R., Paquet A., Nieto J.-L., 1991, *A&A*, 246, 349  
 Bernard E. J., Ferguson A. M. N., Barker M. K., Irwin M. J., Jablonka P., Arimoto N., 2012, *MNRAS*, 426, 3490  
 Bonifacio P., Monai S., Beers T. C., 2000, *AJ*, 120, 2065  
 Butler D. J., Martínez-Delgado D., 2005, *AJ*, 129, 2217  
 Caldwell N., Armandroff T. E., Seitzer P., Da Costa G. S., 1992, *AJ*, 103, 840  
 Conn A. R., Ibata R. A., Lewis G. F., Parker Q. A., Zucker D. B., Martin N. F., McConnachie A. W., Irwin M. J., Tanvir N., Fardal M. A., Ferguson A. M. N., Chapman S. C., Valls-Gabaud D., 2012, *ApJ*, 758, 11  
 Crnojević D., Ferguson A. M. N., Irwin M. J., Bernard E. J., Arimoto N., Jablonka P., Kobayashi C., 2013, *MNRAS*, 432, 832  
 Davidge T. J., 2005, *AJ*, 130, 2087  
 De Rijcke S., Prugniel P., Simien F., Dejonghe H., 2006, *MNRAS*, 369, 1321  
 de Vaucouleurs G., de Vaucouleurs A., Corwin Jr. H. G., Buta R. J., Paturel G., Fouqué P., 1991, *Third Reference Catalogue of Bright Galaxies. Volume I: Explanations and references. Volume II: Data for galaxies between 0<sup>h</sup> and 12<sup>h</sup>. Volume III: Data for galaxies between 12<sup>h</sup> and 24<sup>h</sup>.*  
 Dotter A., Chaboyer B., Jevremović D., Kostov V., Baron E., Ferguson J. W., 2008, *ApJS*, 178, 89  
 Evslin J., 2014, *MNRAS*, 440, 1225  
 Fattahi A., Navarro J. F., Starkenburg E., Barber C. R., McConnachie A. W., 2013, *MNRAS*, 431, L73  
 Geha M., van der Marel R. P., Guhathakurta P., Gilbert K. M., Kalirai J., Kirby E. N., 2010, *ApJ*, 711, 361  
 Gonçalves D. R., Magrini L., Leisy P., Corradi R. L. M., 2007, *MNRAS*, 375, 715  
 Gonçalves D. R., Magrini L., Martins L. P., Teodorescu A. M., Quireza C., 2012, *MNRAS*, 419, 854  
 Grebel E. K., 1997, in Schielicke R. E., ed., *Reviews in Modern Astronomy Vol. 10, Star Formation Histories of Local Group Dwarf Galaxies. (Ludwig Biermann Award Lecture 1996)*. p. 29  
 Grebel E. K., Gallagher III J. S., Harbeck D., 2003, *AJ*, 125, 1926  
 Han M., Hoessel J. G., Gallagher III J. S., Holtsman J., Stetson P. B., 1997, *AJ*, 113, 1001  
 Ho N., Geha M., Tollerud E., Zinn R., Guhathakurta P., Vargas L., 2014, *ArXiv e-prints*  
 Hodge P. W., 1963, *AJ*, 68, 691  
 Hodge P. W., 1976, *AJ*, 81, 25  
 Ibata R. A., Lewis G. F., McConnachie A. W., Martin N. F., Irwin M. J., Ferguson A. M. N., Babul A., Bernard E. J., Chapman S. C., Collins M., Fardal M., Mackey A. D., Navarro J., Peñarrubia J., Rich R. M., Tanvir N., Widrow L., 2014, *ApJ*, 780, 128  
 Irwin M., Lewis J., 2001, *NewA Rev.*, 45, 105  
 Kang A., Sohn Y.-J., Rhee J., Shin M., Chun M.-S., Kim H.-I., 2005, *A&A*, 437, 61  
 Kent S. M., 1987, *AJ*, 94, 306  
 Kim S. C., Lee M. G., 1998, *Journal of Korean Astronomical Society*, 31, 51  
 Koleva M., de Rijcke S., Prugniel P., Zeilinger W. W., Michielsen D., 2009, *MNRAS*, 396, 2133  
 Koleva M., Prugniel P., de Rijcke S., Zeilinger W. W., 2011, *MNRAS*, 417, 1643  
 Leaman R., Venn K. A., Brooks A. M., Battaglia G., Cole A. A., Ibata R. A., Irwin M. J., McConnachie A. W., Mendel J. T., Starkenburg E., Tolstoy E., 2013, *ApJ*, 767, 131  
 Lee M. G., Freedman W. L., Madore B. F., 1993, *AJ*, 106, 964  
 Marcolini A., D'Ercole A., Battaglia G., Gibson B. K., 2008, *MNRAS*, 386, 2173  
 Marleau F. R., Noriega-Crespo A., Misselt K. A., 2010, *ApJ*, 713, 992  
 Martin N. F., Ibata R. A., McConnachie A. W., Dougal Mackey A., Ferguson A. M. N., Irwin M. J., Lewis G. F., Fardal M. A., 2013, *ApJ*, 776, 80  
 Martínez-Delgado D., Aparicio A., Gallart C., 1999, *AJ*, 118, 2229  
 Mateo M. L., 1998, *ARAA*, 36, 435  
 Mayer L., Mastroiello C., Wadsley J., Stadel J., Moore B., 2006, *MNRAS*, 369, 1021  
 McConnachie A. W., Ferguson A. M. N., Irwin M. J., Dubinski J., Widrow L. M., Dotter A., Ibata R., Lewis G. F., 2010, *ApJ*, 723, 1038



- McConnachie A. W., Irwin M. J., Ibata R. A., Dubinski J., Widrow L. M., Martin N. F., Côté P., Dotter A. L., et al. 2009, *Nature*, 461, 66
- McLaughlin D. E., Harris W. E., Hanes D. A., 1994, *ApJ*, 422, 486
- Moore B., Lake G., Katz N., 1998, *ApJ*, 495, 139
- Nowotny W., Kerschbaum F., Olofsson H., Schwarz H. E., 2003, *A&A*, 403, 93
- Pasetto S., Grebel E. K., Berczik P., Chiosi C., Spurzem R., 2011, *A&A*, 525, A99
- Peñarrubia J., Navarro J. F., McConnachie A. W., Martin N. F., 2009, *ApJ*, 698, 222
- Revaz Y., Jablonka P., Sawala T., Hill V., Letarte B., Irwin M., Battaglia G., Helmi A., et al. 2009, *A&A*, 501, 189
- Richardson J. C., Irwin M. J., McConnachie A. W., Martin N. F., Dotter A. L., Ferguson A. M. N., Ibata R. A., Chapman S. C., Lewis G. F., Tanvir N. R., Rich R. M., 2011, *ApJ*, 732, 76
- Robin A. C., Reylé C., Derrière S., Picaud S., 2003, *A&A*, 409, 523
- Sage L. J., Welch G. A., Mitchell G. F., 1998, *ApJ*, 507, 726
- Schlegel D. J., Finkbeiner D. P., Davis M., 1998, *ApJ*, 500, 525
- Schroyen J., De Rijcke S., Koleva M., Cloet-Osselaer A., Vandebroucke B., 2013, *MNRAS*
- Schroyen J., de Rijcke S., Valcke S., Cloet-Osselaer A., Dejonghe H., 2011, *MNRAS*, 416, 601
- Sersic J. L., 1968, *Atlas de galaxies australes*
- Simien F., Prugniel P., 2002, *A&A*, 384, 371
- Spolaor M., Proctor R. N., Forbes D. A., Couch W. J., 2009, *ApJ*, 691, L138
- Stetson P. B., 1987, *PASP*, 99, 191
- Stinson G. S., Dalcanton J. J., Quinn T., Gogarten S. M., Kaufmann T., Wadsley J., 2009, *MNRAS*, 395, 1455
- Teyssier M., Johnston K. V., Kuhlen M., 2012, *MNRAS*, 426, 1808
- Valcke S., de Rijcke S., Dejonghe H., 2008, *MNRAS*, 389, 1111
- van den Bergh S., 1998, *AJ*, 116, 1688
- van den Bergh S., 1999, *A&A Rev.*, 9, 273
- VandenBerg D. A., Bergbusch P. A., Dowler P. D., 2006, *ApJS*, 162, 375
- Veljanoski J., Ferguson A. M. N., Huxor A. P., Mackey A. D., Fishlock C. K., Irwin M. J., Tanvir N., Chapman S. C., Ibata R. A., Lewis G. F., McConnachie A., 2013, *MNRAS*, 435, 3654
- Watkins L. L., Evans N. W., van de Ven G., 2013, *MNRAS*, 430, 971
- Weinberg D. H., Bullock J. S., Governato F., Kuzio de Naray R., Peter A. H. G., 2013, *ArXiv e-prints*